Vinnik, L. P., Kind, R. (1993): Ellipticity of teleseismic S-particle motion. - Geophysical Journal International, 113, 1, pp. 165—170.
DOI: http://doi.org/10.1111/j.1365-246X.1993.tb02537.x

Geophys. J. Int. (1993) **113,** 165–174

Ellipticity of teleseismic *S*-particle motion

L. P. Vinnik[1] and R. Kind[2]

[1] *Institute of Physics of the Earth, Russian Academy of Sciences, B. Gruzinskaya* 10, 123810 *Moscow, Russia*
[2] *GeoForschungsZentrum Potsdam, Telegrafenberg* A6, O-1561 *Potsdam, Germany*

Accepted 1992 September 14. Received 1992 August 4; in original form 1991 June 3

SUMMARY

In the horizontal components of GRF records, particle motions of the teleseismic *S* waves in the period range between 5 and 20 s are usually elliptic. We correct the particle motions for the effect of azimuthal anisotropy at GRF and explain the residual ellipticity by assuming that it is produced at the source side of the wave path by interference of two waves with orthogonal polarizations and differing traveltimes. The estimates of polarization direction of the fast wave and time delay between the waves can be found by analysing the residual particle motion for groups of closely spaced seismic events. The technique was applied to about 40 GRF records of events from the northern and north-western Pacific. In the source regions the *S*-wave pulses propagate in subduction zones. It is found that the surface projections of polarization of the fast wave of the shallow events coincide approximately with the strikes of the corresponding island arcs. This regularity can be explained by anisotropy in the subduction zones provided that the *a* axis of olivine is parallel to the plane of subduction. The fast direction for the deep events in the sea of Japan and the sea of Okhotsk is close to the strike of the Kurile island arc. The time delay between the fast and the slow waves for the deep events is smaller than for the shallow Kurile events (0.9 s versus 1.4 s).

Key words: anisotropy, particle motion, subduction zones, *S* waves.

1 INTRODUCTION

Polarization analysis is a standard method for detecting shear-wave splitting in the earth's medium in a vicinity of the receiver (for a review see Babuška & Cara 1991). Many studies of azimuthal anisotropy in the earth are based on the *SKS* technique where ellipticity of the particle motion in *SKS* phases in the frequency range around 0.1 Hz is caused mainly by shear-wave splitting in the upper mantle under the receiver (e.g. Vinnik, Kosarev & Makeyeva 1984; Kind *et al.* 1985; Silver & Chan 1988; Vinnik, Farra & Romanowicz 1989a; Makeyeva, Plešinger & Horálek 1990; Savage, Silver & Meyer 1990). Application of a similar technique to the broad-band records of the teleseismic *S* phases at the GRF observatory in southern Germany provided evidence of polarization anomalies which could not be easily explained by the properties of the mantle in the receiver region (Vinnik *et al.* 1989b). The purpose of the present study is to isolate and analyse this effect.

The idea of the analysis is as follows: first, we correct the particle motion of the teleseismic *S* phase for anisotropy in the receiver region. This anisotropy is known from the studies based on the *SKS* technique. We describe the residual ellipticity by assuming that it is produced at the source side of the wave path by interference of two *S* waves with orthogonal polarizations and differing traveltimes. It is further assumed that these orthogonal directions and the corresponding traveltime differences are similar for closely spaced seismic events but the particle motions are disturbed by noise. Then estimates of the two parameters can be found by analysing the residual particle motions for groups of closely spaced events. This technique was applied to the records of the events from the northern and north-western margins of the Pacific. Spatial variations of the parameters of ellipticity thus found (especially the fast direction) appear to be closely related to tectonics of the source regions.

2 METHOD

The observations which will be presented in Section 3 indicate that at long periods the particle motion of the teleseismic *S* phase in the horizontal plane is usually elliptic. Most likely, this ellipticity is a cumulative effect of wave propagation in the source and in the receiver regions. Our first objective is to isolate the effect of propagation in the source region provided that the properties of the Earth's medium in the receiver region are known. The particle motion at the bottom of the anisotropic zone in the receiver

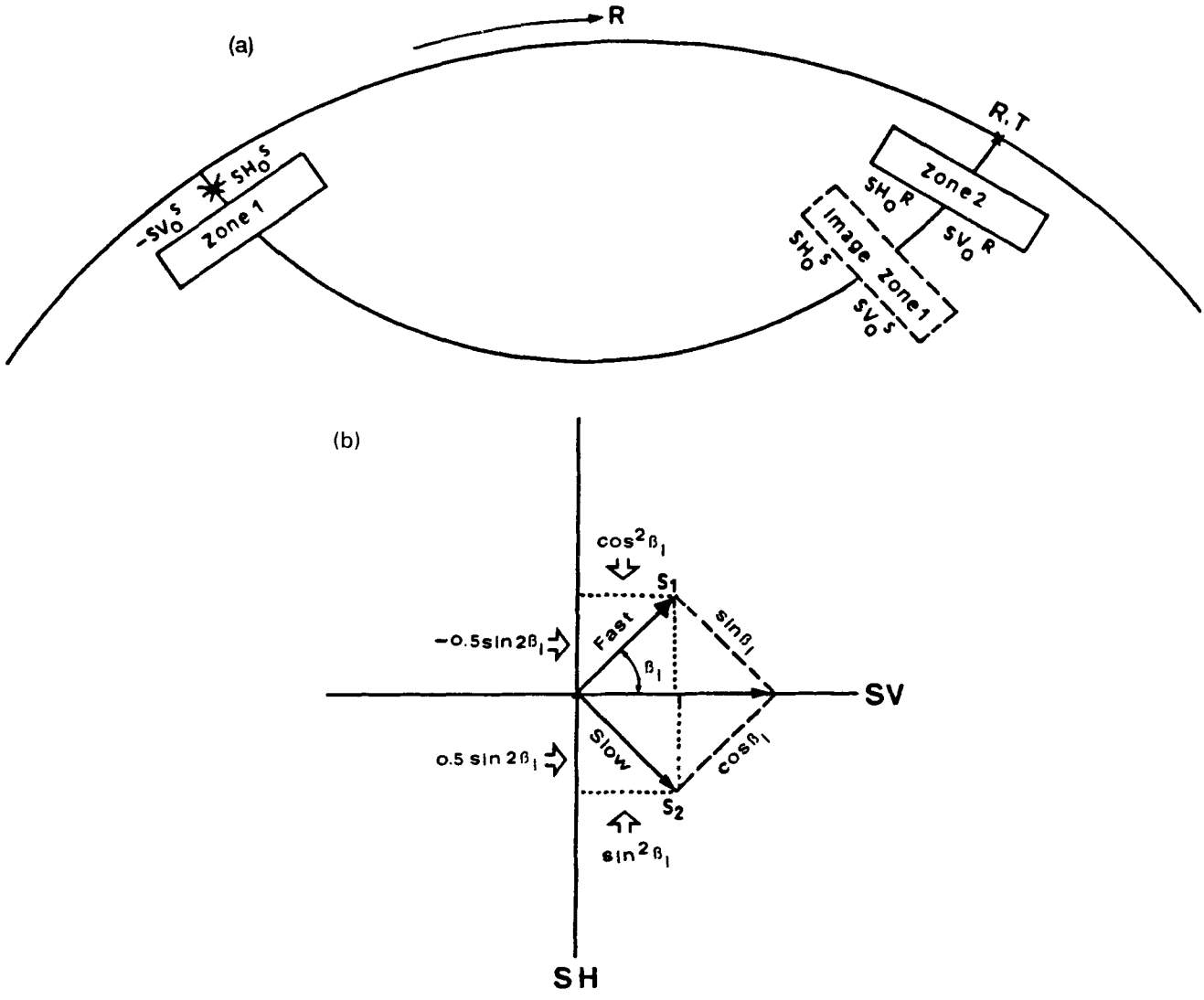

Figure 1. (a) Geometry of the model in the vertical plane containing the direction of propagation, and (b) in a plane perpendicular to the direction propagation.

region can be restored as in the study by Farra *et al.* (1991). We denote by SV_0^R and SH_0^R the *SV* and *SH* components of the incoming *S* wave at the bottom of the zone (zone 2 in Fig. 1a). The horizontal components of the motion recorded at the free surface can be expressed in the frequency domain as:

$$\begin{bmatrix} R(\omega) \\ T(\omega) \end{bmatrix} = F_2(\omega) \begin{bmatrix} SV_0^R(\omega) \\ SH_0^R(\omega) \end{bmatrix} \tag{1}$$

where R and T are the radial and transverse components, and ω is the circular frequency. $F_2(\omega)$ is the matrix of the frequency responses of the anisotropic receiver zone

$$F_2(\omega) = \begin{bmatrix} R_{SV}(\omega) R_{SH}(\omega) \\ T_{SV}(\omega) T_{SH}(\omega) \end{bmatrix}. \tag{2}$$

Using (1), the spectra of the components of the *S* motion at the bottom of the receiver anisotropic zone can be expressed as

$$\begin{bmatrix} SV_0^R(\omega) \\ SH_0^R(\omega) \end{bmatrix} = F_2^{-1}(\omega) \begin{bmatrix} R(\omega) \\ T(\omega) \end{bmatrix}. \tag{3}$$

We adopt a coordinate system where the R axis points in the direction from the source to the receiver. The T axis is oriented with respect to R like *SH* with respect to *SV* in Fig. 1(b). The receiver zone is assumed to be transversly isotropic with a horizontal axis of symmetry, in agreement with Vinnik *et al.* (1989b). β_2 is the angle in the horizontal plane between the fast direction and the R axis. This angle is defined like β_1 in Fig. 1(b), provided that the *SV* axis in Fig. 1(b) is replaced by the R axis. δt_2 is the time delay of the slow split wave with respect to the fast one. Then, following Vinnik *et al.* (1989b), the elements of the matrix (2) can be expressed approximately as

$$\begin{aligned} R_{SV}(\omega) &\approx \cos^2 \beta_2 + \sin^2 \beta_2 \exp(-i\omega\delta t_2) \\ T_{SV}(\omega) = R_{SH}(\omega) &\approx -0.5 \sin 2\beta_2 [1 - \exp(-i\omega\delta t_2)]. \\ T_{SH}(\omega) &\approx \sin^2 \beta_2 + \cos^2 \beta_2 \exp(-i\omega\delta t_2) \end{aligned} \tag{4}$$

The *S* wave generated by a source with a double-couple focal mechanism in a homogeneous isotropic medium is polarized linearly in the far field (Aki & Richards 1980). We assume that if the particle motion at the bottom of the

receiver anisotropic zone is still elliptic, this can be owing to interference of two S waves with orthogonal polarizations and differing traveltimes. This allows us to describe the residual ellipticity by the two parameters: direction of polarization of the fast wave and time delay between arrivals of the waves. It is further assumed that the two S waves are formed at the source side of the wavepath ('zone 1' in Fig. 1a), but, for simplicity of presentation, this zone is replaced by the other one, underneath the receiver anisotropic zone ('image zone 1' in Fig. 1a). The angle between polarization of the fast wave in image zone 1 and axis SV is β_1 (Fig. 1b), and time interval between arrivals of the split waves is δt_1. A relationship between the components of motion at the top of this zone, SV_0^R and SH_0^R, and those at the bottom, SV_0^S and SH_0^S, can be expressed as

$$\begin{bmatrix} SV_0^R(\omega) \\ SH_0^R(\omega) \end{bmatrix} = F_1(\omega) \begin{bmatrix} SV_0^S(\omega) \\ SH_0^S(\omega) \end{bmatrix}$$

where the matrix F_1 can be expressed as

$$F_1(\omega) = \begin{bmatrix} SV_{SV}(\omega) & SV_{SH}(\omega) \\ SH_{SV}(\omega) & SH_{SH}(\omega) \end{bmatrix}.$$

The particle motion at the bottom of the source zone can be restored by using the expression

$$\begin{bmatrix} SV_0^S(\omega) \\ SH_0^S(\omega) \end{bmatrix} = F_1^{-1}(\omega) \begin{bmatrix} SV_0^R(\omega) \\ SH_0^R(\omega) \end{bmatrix}.$$

Assuming that the initial S wave of unit amplitude is polarized as SV, and projecting this vector on the fast ($S1$) and the slow ($S2$) directions, we obtain the following expressions for the amplitudes of the split waves (Fig. 1b):

$$SV_1 = \cos^2 \beta_1, \qquad SV_2 = \sin^2 \beta_1$$

$$SH_1 = -0.5 \sin 2\beta_1, \qquad SH_2 = 0.5 \sin 2\beta_1.$$

Then for the elements of $F_1(\omega)$ we obtain

$$SV_{SV} = \cos^2 \beta_1 + \sin^2 \beta_1 \exp(-i\omega\delta t_1)$$

$$SH_{SV} = -0.5 \sin 2\beta_1 [1 - \exp(-i\omega\delta t_1)].$$

In a similar way, for the incoming SH we obtain

$$SH_{SV} = \sin^2 \beta_1 + \cos^2 \beta_1 \exp(-i\omega\delta t_1).$$

$$SV_{SH} = SH_{SV}.$$

This means that the expressions for $F_1(\omega)$ and $F_2(\omega)$ are similar, except for the differences in β and δt.

In the time domain, the components of the particle motion at the bottom of the image zone 1 can be obtained by inverse Fourier transformation of $SV_0^S(\omega)$ and $SH_0^S(\omega)$ for any trial pair of β_1 and δt_1. The pair $(\beta_1, \delta t_1)$ which provides a linear particle motion may be regarded as an optimum estimate of the parameters. This pair can be found by a grid search over all possible values of the parameters. To evaluate the parameters in the source region (zone 1, Fig. 1a) with respect to the local coordinate system we should restore the source zone in its original position. This can be done by moving image zone 1 backward along the ray and rotating around the T axis so that the incoming S wave always hits the same side of image zone 1. As a result of this rotation the former bottom side of the zone becomes its top side. The sign of the radial motion at the top side, as seen from above, is changed, whereas the T component keeps the sign. To allow for this change the sign of SV used for determining the parameters in zone 1 should be changed.

To quantify linearity of the S-wave particle motion, we use the parameter $l = (\lambda_1/\lambda_2)^{1/2}$ where λ_1 and λ_2 are the minor and major eigenvalues of the corresponding covariance matrix, respectively. This ratio is close to the ratio of the axes of the elliptic curve describing the particle motion (Kanasevich 1981). If the form of the curve varies between a straight line and a circle, then l varies between 0 and 1. The optimum values of β_1 and δt_1 correspond to the minimum of l. To find the optimum parameters from the observations of many events from the same focal region, the values of l can be stacked. The optimum pair $(\beta_1, \delta t_1)$ corresponds to the minimum of $L(\beta_1, \delta t_1) = 1/N\Sigma l(\beta_1, \delta t_1)$, where N is the number of events. Instead of β_1 we use α which is defined as $\alpha = \varphi - \beta_1$, where φ is the azimuth of the receiver with respect to the source. For the waves with steep incidence, like those used in our study, α is close to azimuth of the surface projection of polarization of the fast wave counted clockwise from North.

3 DATA AND RESULTS OF PROCESSING

The procedure described in Section 2 was applied to the records of S in the epicentral distance range between 65° and 80°. The records were obtained at the station A1 of the GRF array. Records at distances larger than 80° are generally not suitable for our purpose, due to possible interference of S with SKS and ScS. At distances much smaller than 65° the linear motion can be disturbed by S-to-P conversions in the lithosphere.

Selecting suitable records is the crucial step in this study. We scanned all GRF records with magnitudes ≥5.7 in the time interval 1983–1990. The search was less systematic for smaller magnitudes and for the years 1977–1982. We selected records with sharp S onsets, stable direction of particle motion during the first cycle of oscillation and a high signal-to-noise ratio. The broad-band velocity output was low-pass filtered to suppress oscillations with periods shorter than about 3–5 s. We have found that at short periods the particle motion becomes more complicated than at longer periods, most likely due to small-scale irregularities of the rupture propagation and small-scale inhomogeneities in the Earth. Sometimes additional low-pass filtering was necessary to provide a good signal-to-noise ratio. Representative examples of the records which were found suitable for further analysis are shown in Figs 2 and 3. These records are also used to demonstrate the relationship between the linearity parameter l and the actual form of the particle motion. A small percentage of the records thus selected (about 10 per cent) was not used in the final inversion of the data since the minimum value of l was too large (more than 0.2). The epicentral parameters of the records used for the inversion are presented in Table 1 and are also plotted in Fig. 4. The values of l were calculated for a grid with increments of 10° for α and 0.2 s for δt.

The next step of our analysis was to test the procedure of Section 2 by applying it to the records of SKS. We have evaluated the parameters of anisotropy in the upper mantle underneath the GRF array using the criterion of linearity of particle motion of SKS. The plot of $L(\alpha, \delta t)$ in Fig. 5 was

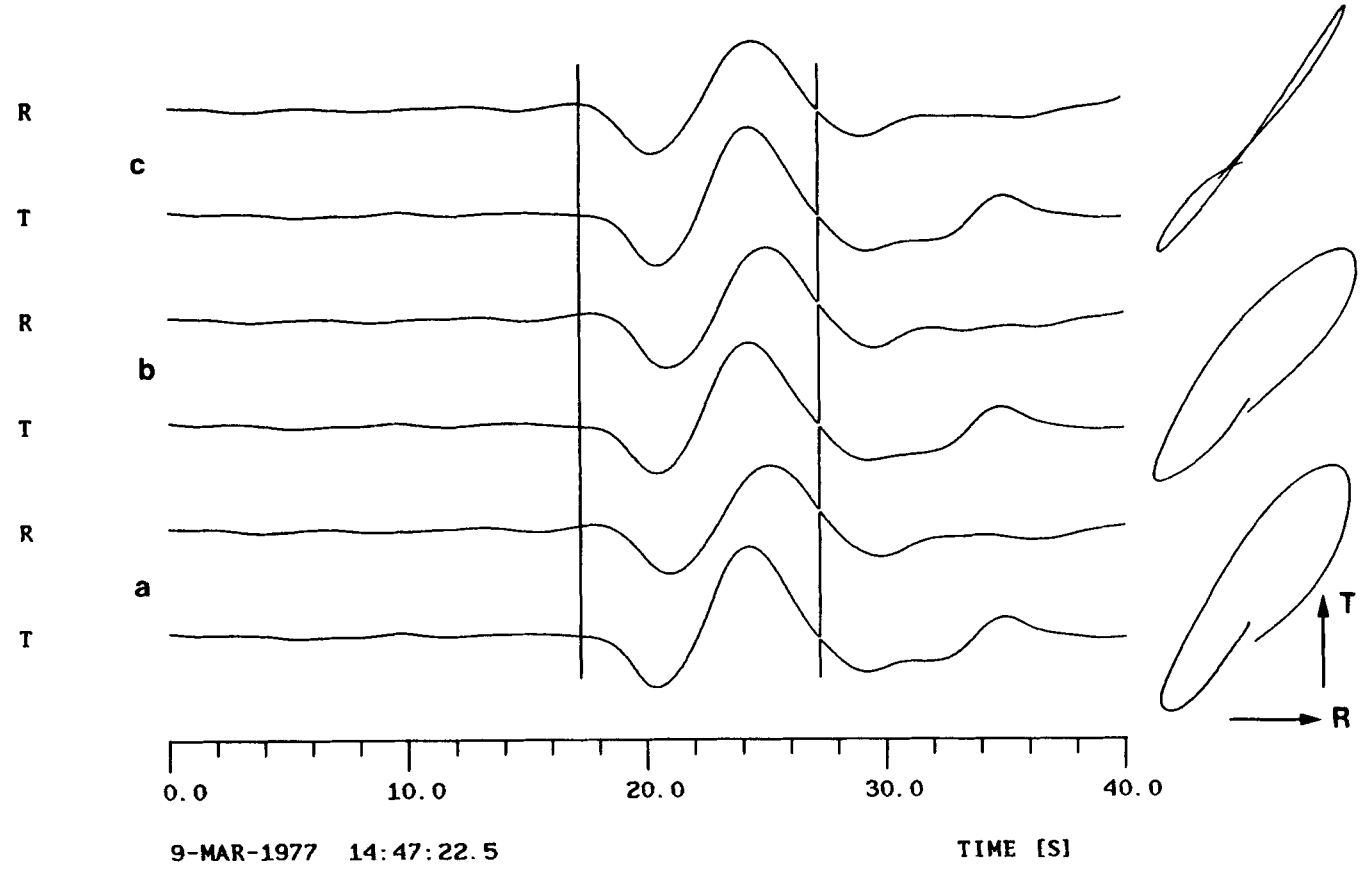

Figure 2. Examples of records and particle motions (event 77.03.09, Table 1). The time interval used for the particle motion plot is indicated by vertical bars. The original broad-band data of the GRF station A1 are low-pass filtered with a cut-off at 5 s. R and T are the radial and transverse components, respectively. The traces (a) are the uncorrected data. The traces (b) are corrected for the receiver anisotropy ($\alpha = 90°$, $\delta t = 0.5$ s). The traces (c) are corrected for the source and receiver anisotropy (for the source $\alpha = 60°$, $\delta t = 0.9$ s). The corresponding values of linearity l are 0.29, 0.27 and 0.04.

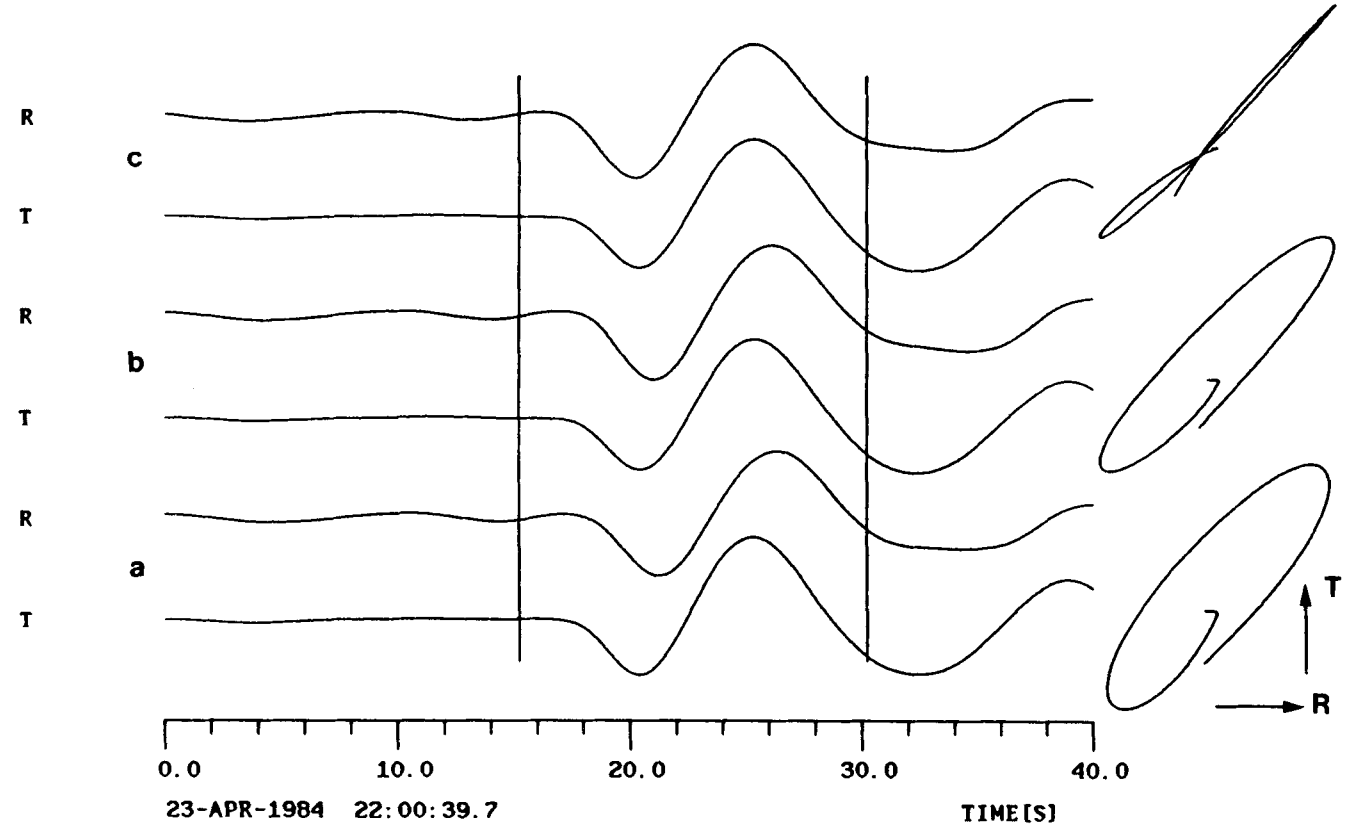

Figure 3. The same as in Fig. 2 for event 84.04.23. A low-pass filter cut-off is at 10 s. The values of l are 0.28, 0.22 and 0.07, respectively.

Table 1. List of events and estimates of α, δt. Epicentres are plotted in Fig. 4.

Date (y.m.d.)	Orig Time (h:m:s)	Epicentre Lat. Lon.(°)	Depth km	mb	Dist (°)	Back Azi (°)	α (°)	δt s
SKS group								
79.05.18	20:18:01.1	24.13n 142.40E	567	5.8	94.9	43.8		
86.05.26	19:06:16.0	20.19s 178.86E	538	6.4	149.3	23.6		
86.09.16	18:56:32.9	19.24n 146.34E	74	5.1	101.0	42.9		
Group No. 1								
77.03.09	14:27:56.2	41.66n 131.05E	556	6.0	75.1	42.4		
79.08.16	21:31:26.3	41.81n 130.78E	588	6.1	74.9	42.4	40	0.7
81.11.27	17:21:45.8	42.91n 131.07E	543	5.9	74.1	41.6		
82.11.27	09:55:38.9	50.20n 147.72E	622	5.7	74.1	27.5		
83.07.24	23:07:31.0	53.93n 158.37E	180	6.2	73.5	19.6	75	1.0
83.10.08	07:45:26.7	44.22n 130.74E	558	5.8	72.9	41.0	50	1.1
84.04.23	21:40:35.5	47.45n 146.69E	414	6.1	76.2	29.5		
87.05.07	03:05:49.2	46.73n 139 23E	430	6.1	74.2	34.4	20	0.7
87.07.14	23:46:03.5	49.63n 147.82E	576	5.8	74.6	27.7		
90.05.12	04:50:09.1	49.04n 141.86E	611	6.4	73.2	31.5		
90.08.20	00:03:52.0	46.20n 142.26E	299	6.0	75.8	32.8		
Group No. 2								
79.07.04	06:07:45.2	43.95n 146.70E	78	6.0	79.3	31.1	120	1.1
81.09.03	05:35:44.8	43.62n 147.03E	45	6.7	79.7	31.1	50	1.4
83.03.10	00:27:48.4	43.81n 147.39E	33	6.3	79.6	30.7	40	1.7
83.05.01	18:10:40.4	46.35n 153.45E	24	6.2	79.2	25.7		
83.06.30	13:39:04.0	44.04n 147.83E	42	5.7	79.6	30.4	15	2.0
84.12.03	04:08:35.1	44.21n 148.13E	65	6.5	79.5	30.1	80	1.4
86.04.16	12:52:16.1	43.89n 147.57E	23	6.4	79.6	30.6	50	1.2
86.06.08	11:02:25.9	43.26n 146.49E	56	6.1	79.8	31.6		
87.01.14	11:03:48.8	42.56n 142.85E	102	6.6	79.1	34.3	40	1.4
Group No. 3								
80.03.22	10:27:40.1	55.70n 161.48E	69	5.7	72.5	17.2		
83.06.09	18:46:00.9	51.41n 174.11W	21	6.3	79.6	3.5	10	0.8
84.11.01	18:43:44.1	55.20n 163.69E	49	5.9	73.4	16.2	75	2.0
85.05.24	22:04:43.4	51.42n 178.43W	34	5.9	79.4	6.2		
85.05.25	23:29:21.7	54.05n 160.99E	46	6.0	73.9	18.1		
86.05.02	10:30:02.8	55.17n 163.84E	15	6.1	73.4	16.1		
86.05.17	16:20:22.2	52.32n 174.50W	26	5.9	78.7	3.7		
87.10.06	20:11:35.1	52.95n 159.97E	34	6.2	74.7	19.1	125	0.6
88.05.25	14:05:17.7	50.54n 174.57W	40	5.8	80.5	3.9		
89.10.07	15:48:30.8	51.28n 179.02W	33	6.1	79.5	6.6		
Group No. 4								
83.02.14	08:10:03.6	54.96n 159.23W	33	6.1	75.9	354.4		
86.06.19	09:09:09.2	56.33n 152.91W	17	6.1	74.0	351.0	70	1.0
86.09.12	23:57:15.6	56.20n 153.40W	31	6.2	74.2	351.2	50	1.6
87.02.27	08:31:54.4	53.47n 167.29W	10	6.3	77.7	359.2		
89.06.16	10:51:21.6	57.75n 153.99W	58	5.9	72.7	351.9	50	1.9
89.09.04	13:15:01.5	55.56n 156.79W	33	6.4	75.1	353.1		
Group No. 5								
83.07.12	15:10:03.4	61.03n 147.28W	37	6.2	68.7	349.1		
83.09.07	19:22:05.2	60.97n 147.50W	45	6.3	68.8	349.1		
88.03.06	22:35:38.1	56.95n 143.03W	10	6.9	72.1	345.6		

obtained from three *SKS* records. The parameters α and δt corresponding to the minimum of L are 90° and 0.8 s, respectively. That means they are practically equal to those obtained previously from the analysis of *SKS* by using a different technique and a larger amount of data (90° and 0.7 s, Vinnik *et al.* 1989b).

To correct the records of *S* for anisotropy in the receiver region we should adopt the values of α and δt for that region. Both values are known from the analysis of *SKS* though the value of δt is somewhat uncertain since the angle of incidence of the teleseismic *S* in the upper mantle (about 25°) is different from that of *SKS* (about 10°). The dependence of the delay on the angle of incidence is defined by the parameter η (see e.g. Dziewonski & Anderson 1981) which is not very well constrained by existing seismic data. The most likely behaviour of the delay as a function of the angle of incidence is a slight decrease with increasing angle in the range between 10° and 30°. The data obtained by Vinnik *et al.* (1989b) from teleseismic *S* at GRF suggest $\delta t = 0.5$ s, which is somewhat less than 0.7 s obtained in the same study from *SKS*. We adopt $\delta t = 0.5$ s as the most likely value for *S*. To demonstrate the effect of the correction as a function of the assumed δt we will further show some results which were obtained on the assumption of $\delta t = 0$.

Plots of $l(\alpha, \delta t)$ for two representative records of *S* (Figs 2 and 3) are shown in Figs 6 and 7. The region of the lowest values of $l(\alpha, \delta t)$ in both examples is U shaped. Large variations of trial values of δt produce relatively small changes in the resulting values of $l(\alpha, \delta t)$ when the principal direction of particle motion of *S* is nearly parallel to the trial direction of polarization of the fast wave or perpendicular to it. A large size of the region of the lowest values of $l(\alpha, \delta t)$ often makes the estimates of the parameters for individual records very uncertain. Stacking $l(\alpha, \delta t)$ for several records may result in a deep and physically meaningful minimum of $L(\alpha, \delta t)$ for a small range of the parameters, as shown by the example for *SKS* in Fig. 5.

To perform stacking, the records of *S* were combined into groups according to their focal coordinates (Fig. 4). Group 1 is composed of the deep events (source depths not less than 180 km) in the region of the sea of Japan and the sea of Okhotsk. Most of the hypocentres are at depths exceeding 400 km. Group 2 is formed by shallow events in the trench near Hokkaido and the Kurile islands. Group 3 is composed of shallow events related to the western part of the Aleutian arc. This group consists of the two clusters, one near Kamchatka and the other between 174°W and 179°W. Solutions for them are compatible with each other, and in order to obtain sufficiently accurate estimates of the parameters, both clusters were combined in a single group. Group 4 is formed by a cluster of shallow events near the eastern segment of the Aleutian arc. There is also small Group 5 of events in the Gulf of Alaska.

In Fig. 8 we present the plot $L(\alpha, \delta t)$ for Group 1. $L(\alpha, \delta t)$ has its minimum (around 0.1) at $\alpha = 60°$ and $\delta t = 0.9$ s. In this group we have four events with individual estimates of the parameters (Table 1). All estimates of α are between 20° and 75°. The standard error σ of the minimum value of $L(\alpha, \delta t)$ is 0.01. Rough statistical estimates of the errors of the optimum values of α and δt can be obtained by considering the size of the part of the diagram bordered by the line $L_{\min} + \sigma$. In our case the errors of α and δt are of the order of 10° and 0.2 s, respectively. The errors for the other groups (except Group 5) are of the same order of magnitude. Finally we note that the found fast direction practically coincides with the strike of the Kurile island chain (see Fig. 4).

For comparison the plot $L(\alpha, \delta t)$ for Group 1, computed with the assumption $\delta t = 0$ in the receiver region, is shown in Fig. 9. In this case the optimum values of the parameters are $\alpha = 70°$ and $\delta t = 1.3$ s. The change with respect to the data shown in Fig. 6 is clearly small, especially for α. Similar small changes were also observed in the results for the other groups. The small effect of the allowance for the receiver anisotropy can partly be explained by the fact that the principal direction of the *S*-particle motion at the receiver is often nearly parallel or perpendicular to the E–W direction of the axis of symmetry (fast velocity at the GRF array). We conclude that an error of about 0.3 s in the assumed δt for the receiver region (which is probably the largest possible error) can not introduce significant errors in our final results.

The result of processing the records of Group 2 is presented in Fig. 10. The estimates of α and δt are 55° and 1.4 s, respectively. Individual estimates are available for the majority of events in this group (Table 1). Almost all values of α, except one, are between 15° and 80°. The fast direction

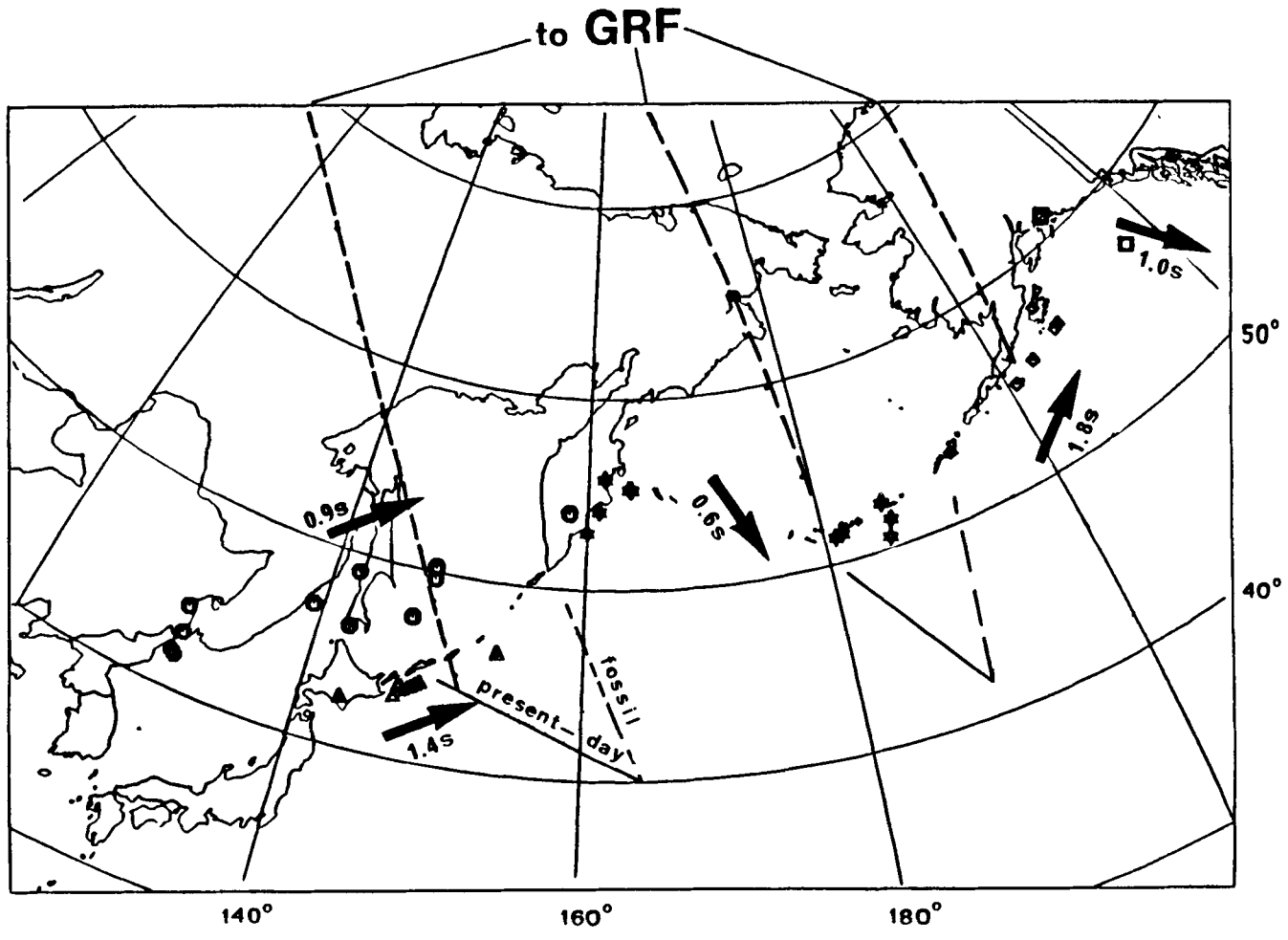

Figure 4. Location map of the events used (see Table 1). Circles are the deep events of Group 1, triangles are Group 2, stars Group 3, diamonds Group 4, and squares are Group 5. For definition of groups, see text. Arrows mark surface projections of the fast-wave polarization for each group, the numbers attached to the arrows indicate estimates of δt. Fossil and present-day absolute plate-velocity directions of the Pacific plate are after Nishmura & Forsyth (1989).

practically coincides with the direction found from the records of the deep events and also with the strike of the Kurile island chain.

The data for the region of the Aleutian islands (Groups 3 and 4) are presented in Figs 11 and 12. Only three individual estimates are available for Group 3 which consists of 10 events. The values of α are strongly scattered. Three individual estimates are also available for Group 4 which consists of six events. The individual values of α are between 50° and 70°. The plots of $L(\alpha, \delta t)$ indicate statistically significant differences between the groups. The most likely fast direction for Group 3 (western segment of the arc) is 140°–150° and $\delta t = 0.6$ s. In the eastern segment (Group 4) the direction is 50° and $\delta t = 1.8$ s. The estimate of δt is somewhat uncertain, but the minimum of $L(\alpha, \delta t)$ for α is very narrow. We note that in both cases the fast direction, like in the Kurile region, follows the local strike of the island arc.

Finally, in Fig. 13 we present data for the small Group 5 of events in the Gulf of Alaska. In this case the estimates of the parameters are less well constrained than in the other groups. The preferred fast direction of 150° is nearly parallel to the sea shore and the corresponding mountain ranges, δt is about 1 s.

DISCUSSION AND CONCLUSIONS

Our results can shortly be summarized as follows. We presented evidence that ellipticity of the teleseismic S-particle motion often can not be explained by azimuthal anisotropy in the receiver region, and introduced a technique of analysis of the residual ellipticity. We assume that the residual ellipticity is formed at the source side of the wave path and is caused by splitting of the initial linearly polarized wave into two orthogonally polarized shear waves. The technique was applied to the GRF recordings of events from the northern and north-western Pacific. The projections of the fast-wave polarization direction thus found for all shallow events are close to the local strikes of the arcs. The fast direction for the deep events in the sea of Japan and the sea of Okhotsk practically coincides with the direction for the shallow Kurile events. The value of δt for the deep events is smaller than for the shallow Kurile events (0.9 s versus 1.4 s).

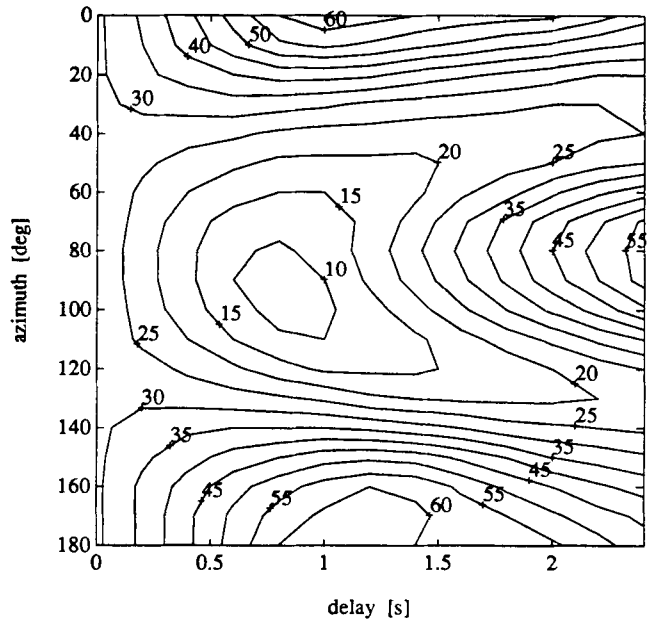

Figure 5. Contours of $L(\alpha, \delta t)$ for estimating the parameters of receiver anisotropy at GRF using the criterion of linearity of *SKS*. The values of L in this and the other figures have been multiplied by 100. The records of *SKS* are listed in Table 1. The optimum values of the parameters correspond to the minimum of L.

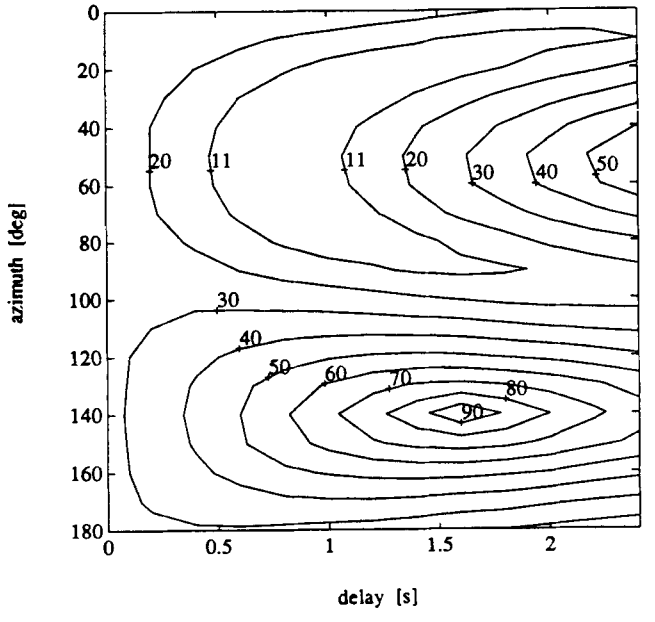

Figure 6. Contours of $l(\alpha, \delta t)$ for event 77.03.09.

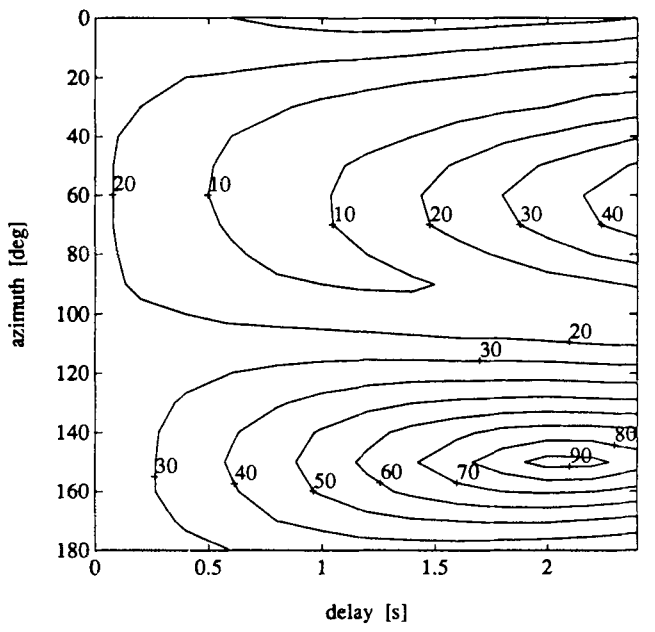

Figure 7. The same as in Fig. 6 for event 84.04.23.

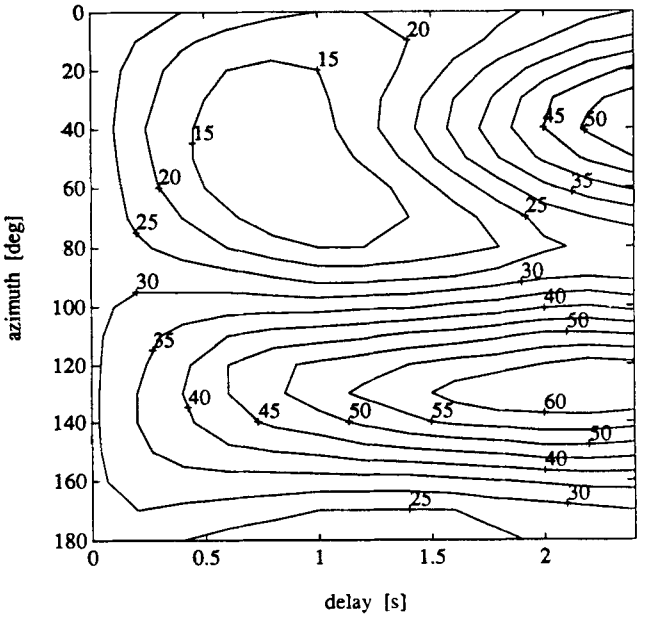

Figure 8. Contours of $L(\alpha, \delta t)$ for estimating the parameters of source anisotropy for Group 1 (deep events from the sea of Japan and the sea of Okhotsk). The optimum values of the parameters correspond to the minimum of L.

The technique is formulated without strong assumptions about the origin of splitting. The difficulty of defining the origin of splitting stems mainly from the fact that the *S*-wave pulses on their way to the GRF observatory propagate within and near the subducted slabs (Fig. 4), whereas theoretical and modelling results for wavefields in the structures of a similar complexity are still not elaborate enough to be compared with the observations. In the discussion which follows we compare various ways of interpreting our data and try to find the most convincing explanation of them.

One of the possible reasons for the observed ellipticity is anisotropy in the mantle of the source regions. Evidence of the upper mantle anisotropy was previously found in practically every region of the earth where a suitable analysis of data was performed. Our estimates of δt are in the range of values reported for mantle anisotropy in the other regions. If the upper mantle in the source region is anisotropic with arbitrary symmetry and orientation of axes, then the initial *S*-wave pulse splits into two orthogonally polarized quasi-shear waves which propagate with different velocities, in agreement with our assumptions. There are

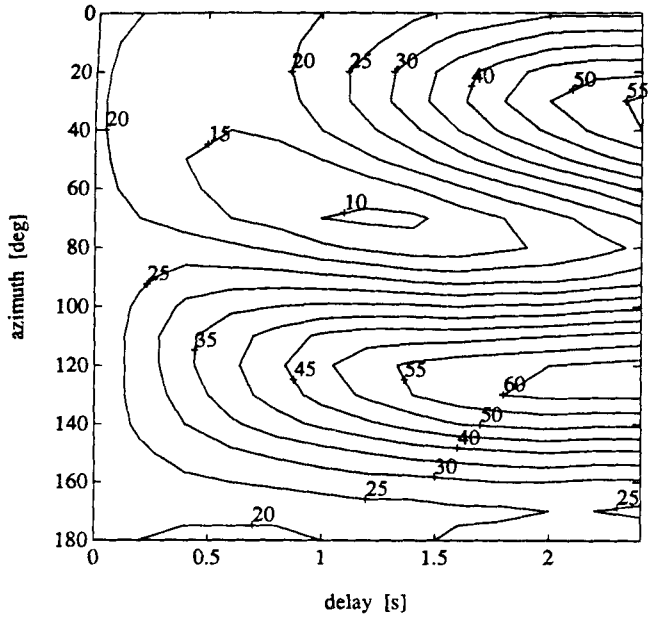

Figure 9. The same as in Fig. 8 without correction for the receiver anisotropy.

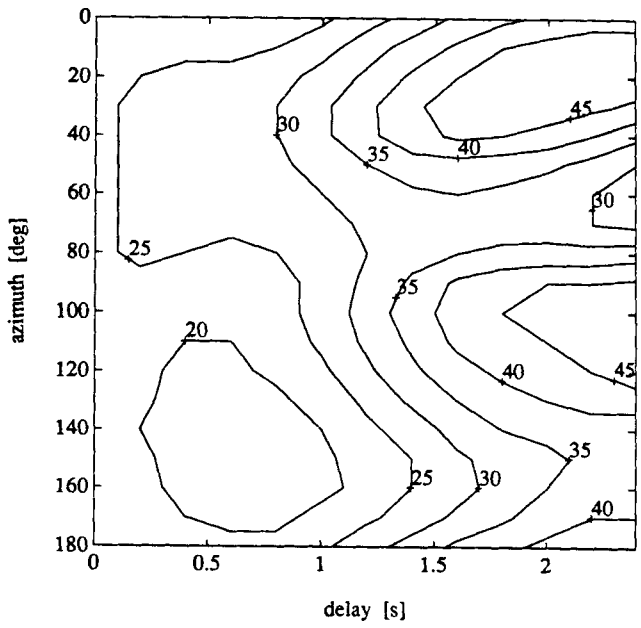

Figure 11. The same as in Fig. 8 for Group 3 (Komandorsky and western Aleutian island arc).

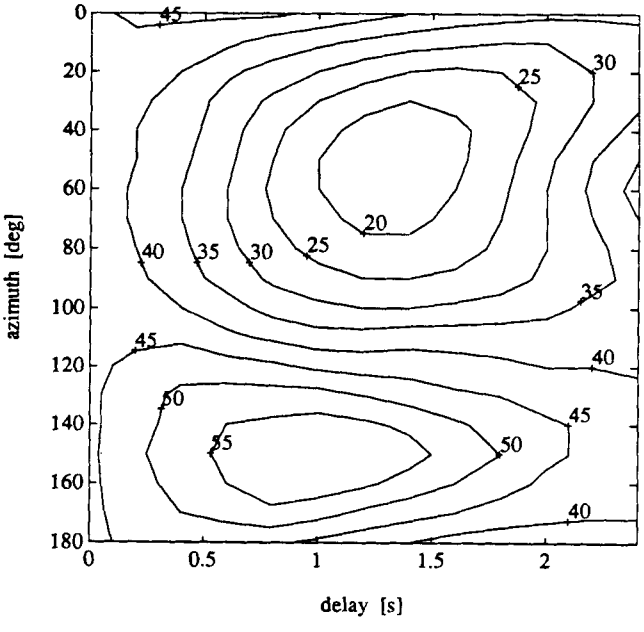

Figure 10. The same as in Fig. 8 for Group 2 (shallow events near Hokkaido and the Kuriles).

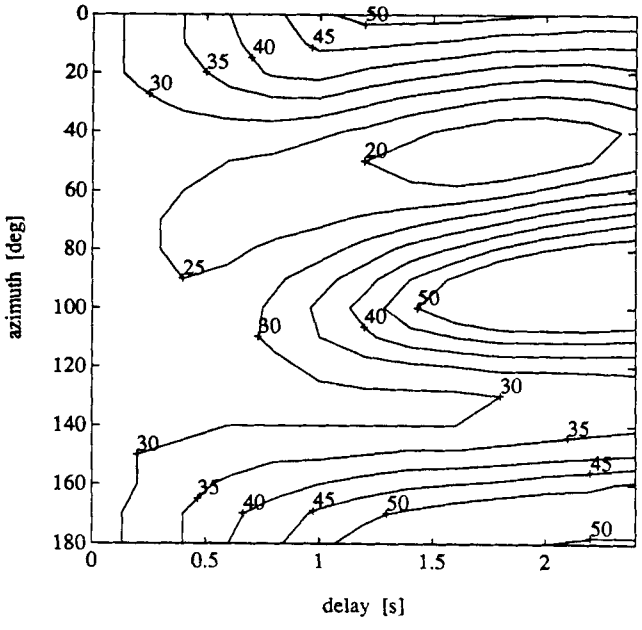

Figure 12. The same as in Fig. 8 for Group 4 (eastern Aleutian island arc).

theoretical predictions and observational results for anisotropy in the subduction zones and we will examine whether our results are compatible with them.

It is well known that in the upper most part of the oceanic mantle, anisotropy is frozen with the α axis of olivine pointing in the fossil spreading direction (e.g. Shimamura *et al.* 1983). This direction in the Pacific is shown in Fig. 4. Results of the inversion of the *P* traveltimes in Japan by Hirahara & Ishikawa (1984) suggest that frozen anisotropy of the suboceanic lithosphere is preserved in the subducted slab. According to Babuška & Cara (1991) frozen anisotropy may be present in subducted slabs down to depths of at least 400 km. Shear strain in the mantle above the sinking slab is another candidate mechanism producing anisotropy (McKenzie 1979; Ribe 1989). In that case the olivine axis *a* aligns with the direction of motion of the slab. Then anisotropy in the subduction zones is a combined effect of frozen anisotropy in the descending slabs and of finite strain associated with subduction.

We assume that the directions of wave propagation in the source regions are parallel to the slabs. That means that both the olivine axis *a* and the direction of wave propagation

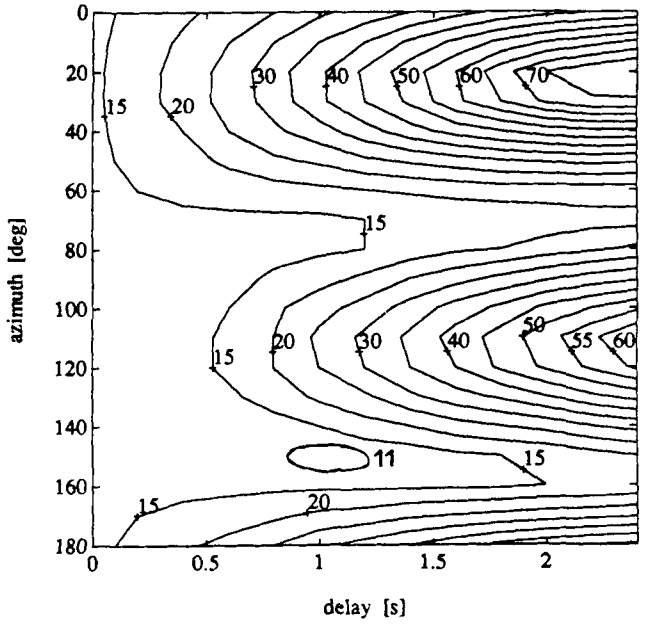

Figure 13. The same as in Fig. 8 for Group 5 (Gulf of Alaska).

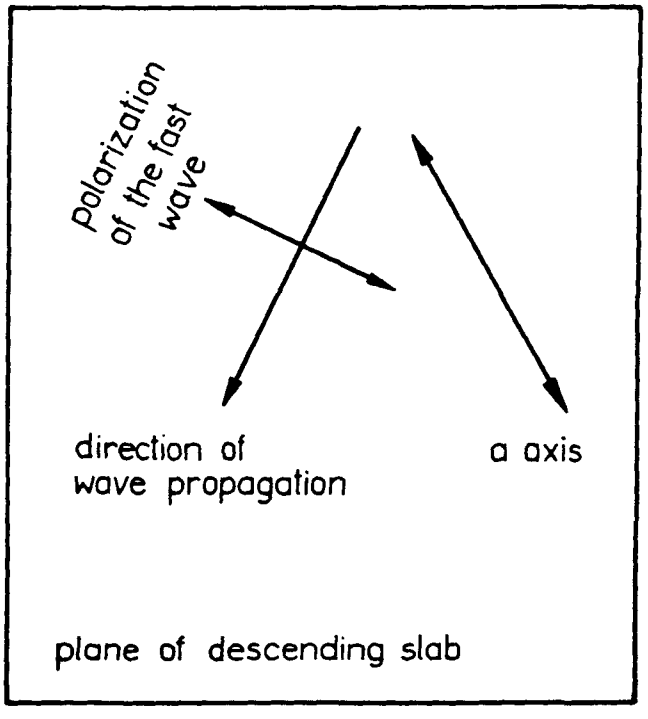

Figure 14. Sketch illustrating the relationship between wave propagation direction, orientation of the *a* axis and polarization of the fast wave in the plane of descending slab.

are in the same plane coinciding with the plane of the slab (Fig. 14). We assume that anisotropy in the subduction zone is hexagonal with the symmetry axis coinciding with the *a* axis of olivine. This simple model describes the properties of the upper mantle rocks with sufficient accuracy (e.g. Estey & Douglas 1986; Kawasaki 1986). It follows from the properties of the corresponding Christoffel matrix that the vector of polarization of the slow wave is perpendicular to the *a* axis. This vector is also perpendicular to the direction of wave propagation and consequently to the plane of subduction. Then the polarization vector of the fast wave is in the plane of subduction, as shown in Fig. 14. This can explain why the projection of the fast-wave polarization direction in Fig. 4 follows the strike of the subduction zones.

When the direction of wave propagation is parallel to the *a* axis there is no splitting. The projections of the direction of wave propagation in Fig. 4 are almost parallel to the fossil spreading direction implying that the direction of wave propagation in the subduction zones is almost parallel to the *a* axis of frozen anisotropy and that contribution of frozen anisotropy to the observed ellipticity should be small. The angle between the projections of wave propagation direction and the direction of present-day plate motion is in the range of 30°–50° (Fig. 4) implying that the effect of recently formed anisotropy in the subduction zones can be dominant in our data. Finally, we note that the observed alignment of the fast direction with the strike of the subduction zones resembles very closely the phenomenon found in a number of collisional belts where the fast direction with the strike of the subduction zones resembles very closely the phenomenon found in a number of collisional belts where the fast direction aligns with the axis of the belt or the plate boundary (Vinnik *et al.* 1992).

The data for the deep events deserve special discussion. Anisotropy at depths exceeding 400 km could be due to crystal alignment of silicate spinel. The magnitude of the velocity difference between the split waves in this rock can be in the range of several per cent (Fujimura 1984), which is sufficient for explaining the observed effect. This anisotropy could have bearings on the problems of structure, composition and processes in the lowest parts of the subduction zones (e.g. van der Hilst *et al.* 1991).

Another reason for the observed ellipticity of the *S*-particle motion could be heterogeneity of the upper mantle in the subduction zones. A similar trade-off between azimuthal anisotropy and heterogeneity is characteristic of other seismic techniques (Babuška & Cara 1991). The directions of wave propagation in Groups 1 and 2 are close to the dip direction of the corresponding slab implying that the oscillations in the *SH* and *SV* waves are either in the planes of subducted slabs (*SH*) or perpendicular to them (*SV*). The polarization directions of the fast wave in these groups can be interpreted as an indication that *SH* is faster than *SV*. Such differences are common for the wavefields in heterogeneous media where diffraction or guided-wave propagation are involved. However, the merits of this interpretation are somewhat invalidated by the observation that the fast wave in Group 3, contrary to the Groups 1 and 2, is close to *SV*. This interpretation is further complicated by the observation (Schwartz *et al.* 1991) that slab velocity heterogeneity may be relatively weak in the depth range sampled by the data of Group 1.

In principle, the observed effects could be caused by heterogeneities not only in the source regions but also in the lower mantle between the source and the receiver. There is evidence of structural complexity at the base of the mantle near the wave-path between the Kurile island region and the GFR array (Weber & Davis 1990). However, a relationship between the direction of fast polarization and the local tectonics suggests that ellipticity is indeed produced in the

source region rather than somewhere else. We also evaluated by numerical experiments the deviations from linearity in the *S* waves reflected at the mantle discontinuities in the near-critical range, and have found that these effects are small enough to be neglected.

Our technique of data analysis assumes that the *S*-wave motion in the source is linear. This is true for the double-couple point source in the isotropic medium. Observations, however, indicate that the focal mechanisms of strong seismic events often deviate from double-couple. For example, they may contain an additional, so-called CLVD component (e.g. Sipkin 1986). Among other reasons, this component could be caused by ruptures occuring on a few different fault planes or on a non-planar fault surface. Additional complexity can be caused by faulting of anisotropic media (Kawasaki & Tanimoto 1981). We avoided some of the possible complications by using only the initial part of the *S*-wave recordings and by selecting the records with the simplest pattern of particle motion, like those shown in Figs 2 and 3. Some other unwanted effects are of random nature and, probably, averaged out by stacking the data for many events.

To conclude, we presented observational evidence of the effect which is fairly systematic in the groups of closely spaced events but is largely neglected in previous seismic studies. Unambiguous physical interpretation of this effect requires further observational and theoretical research but the most successful explanation of the data in our disposal is provided by interpreting them in terms of anisotropy in the source region.

ACKNOWLEDGMENTS

This research was supported by the Deutsche Forschungsgemeinschaft and the Kernforschungszentrum Karlsruhe. The authors appreciate a discussion of the subject with V. Farra as well as the comments from G. Mueller, D. Gajewski and an anonymous reviewer. We also wish to thank Jan Wüster for support in generating the plots. Most of this research was carried out at the Seismologisches Zentralobservatorium Gräfenberg, where the first author (LPV) was working as a visiting scientist, and the second (RK) as a member of the staff.

REFERENCES

Aki, K. & Richards, P. G., 1980. *Quantitative Seismology: Theory and Methods*, Freeman & Co, San Francisco.

Babuška & Cara, M., 1991. *Seismic anisotropy in the Earth*, Kluwer Academic Publishers, Dordrecht.

Dziewonski, A. M. & Anderson, D. L., 1981. Preliminary Reference Earth Model, *Phys. Earth planet. Interiors*, **25**, 297–356.

Estey, L. H. & Douglas, B. J., 1986. Upper-mantle anisotropy: a preliminary model, *J. geophys. Res.*, **91**, 11 393–11 406.

Farra, V., Vinnik, L. P., Romanowicz, B., Kosarev, G. L. & Kind, R., 1991. Inversion of teleseismic *S*-particle motion for azimuthal anisotropy in the lithosphere: a feasibility study, *Geophys. J. Int.*, **106**, 421–431.

Fujimura, A., 1984. Preferred orientation of silicate spinel inferred from experimentally deformed aggregates of trevorite, *J. Phys. Earth*, **32**, 273–297.

Hirahara, K. & Ishikawa, Y., 1984. Travel time inversion for three-dimensional *P*-wave velocity anisotropy, *J. Phys. Earth*, **32**, 197–218.

Kanasevich, E. R., 1981. *Time sequence analysis in Geophysics*, The University of Alberta Press, Edmonton.

Kawasaki, I. & Tanimoto, T., 1981. Radiation patterns of body waves due to the seismic dislocation occuring in an anisotropic medium, *Bull. seism. Soc. Am.*, **71**, 37–50.

Kawasaki, I., 1986. Azimuthally anisotropic model of the oceanic upper mantle, *Phys. Earth planet. Interiors*, **43**, 1–21.

Kind, R., Kosarev, G. L., Makeyeva, L. I. & Vinnik, L. P., 1985. Observations of laterally inhomogeneous anisotropy in the continental lithosphere, *Nature*, **318**, 358–361.

McKenzie, D., 1979. Finite deformation during fluid flow, *Geophys. J. R. astr. Soc.*, **58**, 689–671.

Makeyeva, L. I., Plešinger, A. & Horálek, J., 1990. Azimuthal anisotropy beneath the Bohemiam Massif from broadband seismograms of *SKS* waves, *Phys. Earth planet. Interiors*, **62**, 298–306.

Nishimura, C. E. & Forsyth, D. W., 1989. The anisotropic structure of the upper mantle in the Pacific, *Geophys. J. Int.*, **96**, 203–229.

Ribe, N. M., 1989. Seismic anisotropy and mantle flows, *J. geophys. Res.*, **94**, (No. B4), 4213–4223.

Savage, M. K., Silver, P. G. & Meyer, R. P., 1990. Observations of teleseismic shear-wave splitting in the Basin and Range from portable and permanent stations, *Geophys. Res. Lett.*, **17**, 21–24.

Schwartz, S. Y., Lay, T. & Grand, S. P., 1991. Seismic imaging of subducted slabs: trade-offs with deep path and near-receiver effects, *Geophys. Res. Lett.*, **18**, 1265–1268.

Shimamura, H., Asada, T., Suyehiro, K., Yamada, T. & Inatani, H., 1983. Longshot experiments to study velocity anisotropy in the oceanic lithosphere of the northwestern Pacific, *Phys. Earth planet. Interiors*, **31**, 348–362.

Silver, P. & Chan, W. W., 1988. Implications for continental structure and evolution from seismic anisotropy, *Nature*, **355**, 34–39.

Sipkin, S. A., 1986. Interpretation of non-double-couple earthquake mechanisms derived from moment tensor inversion, *J. geophys. Res.*, **91**, 531–547.

van der Hilst, R., Engdahl, R., Spakman, W. & Nolet, G., 1991. Tomographic imaging of subducted lithosphere below the northwest Pacific island arcs, *Nature*, **353**.

Vinnik, L. P., Kosarev, G. L. & Makeyeva, L. I., 1984. Anisotropy of the lithosphere from the observations of *SKS* and *SKKS*, *Proc. Acad. Sci. USSR*, **78**, 1335–1339 (in Russian).

Vinnik, L. P., Farra, V. & Romanowicz, B., 1989a. Azimuthal anisotropy in the Earth from observations of *SKS* at Geoscope and NARS broadband stations, *Bull. Seism. Soc. Am.*, **79**, 1542–1558.

Vinnik, L. P., Kind, R., Kosarev, G. L. & Makeyeva, L. I., 1989b. Azimuthal anisotropy in the lithosphere from the observations of long-period *S* waves *Geophys. J. Int.*, **99**, 549–559.

Vinnik, L. P., Makeyeva, L. I., Milev, A. & Yu. Usenko, A., 1992. Global patterns of azimuthal anisotropy and deformations in the continental mantle, *Geophys. J. Int.*, **111**, 433–447.

Weber, M. & Davis, J. P., 1990. Evidence of laterally variable lower mantle structure from *P* and *S* waves, *Geophys. J. Int.*, **102**, 231–255.